

Merging numerical renormalization group and intermediate representation to compactify two- and three-point correlators

Sebastian Huber, Markus Wallerberger, Paul Worm, and Karsten Held

Institute of Solid State Physics, TU Wien, 1040 Vienna, Austria

(Dated: July 6, 2022)

The vanguard of many-body theory is nowadays dealing with the full frequency dynamics of n -point Green's functions for n higher than two. Numerically, these objects easily become a memory bottleneck, even when working with discrete imaginary-time Matsubara frequencies. Here, we use the intermediate representation (IR) to compactify the two-point Green's function and three-point Fermion-Bose vertex directly on the real frequency axis, on the basis of numerical renormalization group (NRG) data. We empirically observe an upper bound of the relative error when comparing the IR reconstructed signal with the original NRG data, and demonstrate that a IR compaction is possible.

I. INTRODUCTION

Many-body n -point Green's functions are at the very core of quantum field theory [1, 2]. Its two-point variant describes the propagation of a single particle, which may be strongly renormalized or even indicate a Mott metal-insulator transition due to strong interactions [3, 4]. The three-point Green's function describes the coupling of three bosons or that of fermions to bosonic degrees of freedom. An example is the coupling of electrons to spin fluctuations, which, among others, is of relevance for the physics of high-temperature superconductivity [5–8]. The four-point fermionic Green's function, in turn, is connected to physical response functions. An example is the optical conductivity which may show various vertex corrections, such as excitons [9, 10], weak-localization corrections [11] and π -tons [12].

Such n -point Green's functions or the associated vertex functions also form the backbone of dynamical mean-field theory (DMFT) [13–16] and diagrammatic extensions thereof [17–19]. Specifically, DMFT is closely connected to the two-point (one-particle) Green's function or the associated vertex, the self-energy, which are determined self-consistently within the DMFT cycle [14]. Diagrammatic extensions are either based on the four-point vertex [17, 18], where the three-point vertex enters additionally for solving the Bethe-Salpeter equation efficiently [20, 21], or on the three-point vertex directly [22, 23]. Also tiling a major part of the non-local correlations with three-point vertices and including the residual four-point vertex in the parquet equations is possible [24, 25].

These three-point (and even more so the four-point) correlators easily become huge objects in the full parquet version of the diagrammatic extensions of DMFT [26, 27], where they depend on two (three) frequencies and momenta. Momentum is discretized within the Brillouin zone, and frequencies are discretized at Matsubara frequencies. Despite using a truncated-unity expansion for the momenta [28] and the high-frequency asymptotics for the frequencies [27, 29], memory access quickly becomes the computational bottleneck.

A breakthrough to overcome this obstacle was recently achieved using the intermediate representation (IR) [30, 31] which is based on the rapid decay of singular values of the integration kernel for the spectral representation in terms of Matsubara frequencies. At the same time, pioneering work

using the numerical renormalization group (NRG) [32, 33] allowed, for the first time, the calculation of the full real-frequency dynamics of the four-point correlator for a single impurity Anderson model (SIAM). This four-point Green's function or the associated vertex constitute the starting point for the aforementioned diagrammatic extensions of DMFT.

In this paper, we compactify NRG data for the two- and three-point Green's function in the IR basis. Starting point is the representation of the n -point time-ordered correlation functions as a sum of integrals convolving kernel functions and spectral densities. We further demonstrate that the IR basis cannot only be employed on the Matsubara axis but also on the real frequency axis.

The outline of the paper is as follows: In Section II the general representation of the n -point Green's function in terms of spectral densities and Kernel functions is recapitulated, before turning to the specific spectral representation of the two- and three-point correlator which are at the focus of the present paper. Section III provides some information on the SIAM model and NRG method. In Section IV, the NRG calculation of the two-point Green's function and three-point Fermi-Bose vertex is validated against the exact result in the atomic limit and numerical quantum Monte Carlo (QMC) data for a finite hybridization, including an analysis of the error. Section V briefly recapitulates the IR. In Section VI we present our key results, the IR representation of the NRG two- and three-point correlator on the real axis. Section VII further demonstrates the compactification, using real-frequency data as a starting point. Finally, Section VIII provides a summary.

II. SPECTRAL DENSITY REPRESENTATION OF TWO- AND THREE-POINT FERMIONIC CORRELATORS

Let us presume the reader is familiar with the Matsubara and imaginary time formalism of quantum field theory [1] and define the n -point fermionic imaginary-time Green's function

$$\mathcal{G}(\tau_1, \dots, \tau_n) = (-1)^{n-1} \langle T_\tau A_1(\tau_1) \cdots A_n(\tau_n) \rangle, \quad (1)$$

where the Wick operator T_τ orders the fermionic operators $A_i(\tau_i) = e^{H\tau_i} A_i e^{-H\tau_i}$ with $0 \leq \tau_i < \beta = 1/T$ in descending chronology (with an additional minus sign for an odd permutation). For time-translational invariant systems, we can set

$\tau_n = 0$ as reference time and the Green's function reduces to

$$G(\tau_1, \dots, \tau_{n-1}) = (-1)^{n-1} \langle T_\tau \left(\prod_{i=1}^{n-1} A_i(\tau_i) \right) A_n \rangle. \quad (2)$$

We follow hereby the notation of Ref. [32] using a calligraphic symbol in order to refer to the full n -point object, while a roman symbol for a correlator with $n - 1$ independent arguments. The time-ordered product can be formally expanded into a sum over permutations $S_{n-1} = \{\sigma_1, \sigma_2, \dots, \sigma_{(n-1)!}\}$ of the time indices:

$$\begin{aligned} T_\tau \left(\prod_{i=1}^{n-1} A_i(\tau_i) \right) \\ = \sum_{j=1}^{(n-1)!} \text{sgn}(\sigma_j) \left(\prod_{i=1}^{n-2} \theta(\tau_{\sigma_j(i)} - \tau_{\sigma_j(i+1)}) \right) \left(\prod_{i=1}^{n-1} A_{\sigma_j(i)}(\tau_{\sigma_j(i)}) \right), \end{aligned} \quad (3)$$

where by $\sigma_j(i)$ we denote the place of the i -th index in the j -th permutation. Note that all addends except for the chronologically ordered one are zero because of the Heaviside functions. This expression can be further rearranged into kernel and spectral functions as follows (for a detailed derivation via the Lehmann representation see Appendix A)

$$\begin{aligned} G(\tau_1, \dots, \tau_{n-1}) = \sum_{j=1}^{(n-1)!} \text{sgn}(\sigma_j) \int d^{n-1} \epsilon \\ \times K_j(\tau_1, \dots, \tau_{n-1}; \epsilon_1, \dots, \epsilon_{n-1}) \rho_j(\epsilon_1, \dots, \epsilon_{n-1}), \end{aligned} \quad (4)$$

since each permutation comes with a kernel function:

$$\begin{aligned} K_j(\tau_1, \dots, \tau_{n-1}; \epsilon_1, \dots, \epsilon_{n-1}) \\ = (-1)^{n-1} \left(\prod_{i=1}^{n-2} \theta(\tau_{\sigma_j(i)} - \tau_{\sigma_j(i+1)}) e^{-\epsilon_i \tau_{\sigma_j(i)}} \right) e^{-\epsilon_{n-1} \tau_{\sigma_j(n-1)}}, \end{aligned} \quad (5)$$

convoluted with an associated spectral density:

$$\rho_j(\epsilon_1, \dots, \epsilon_{n-1}) = \int d^n t \left\langle \left(\prod_{i=1}^{n-1} A_{\sigma_j(i)}(t_i) e^{i\epsilon_i t_i} \right) A_n \right\rangle. \quad (6)$$

Here ϵ_i stands for excitation energies between two eigenstates (cf. Appendix A), and the $d^{n-1} \epsilon$ and dt^{n-1} integrations merely warrant $t_i = \tau_{\sigma_j(i)}$ reproducing the original Eqs. (2), (3). This arrangement is very similar to Eq. (34a) ff. in Ref. [32] except that we decompose here the time-translational invariant correlator and introduce an energy integral $d^{n-1} \epsilon$ to imply the connection to the spectral functions consisting of weights and excitations (similar to Eq. (28) in Ref. [32]). Such a separation of the full Green's function into the product of kernels and spectral densities has been pointed out already in Ref. [34]. The Green's function Eq. (1) and kernel Eq. (5), which consists of exponentially damped Heaviside step functions, are represented in Matsubara frequency notation using a Fourier transformation

$$G(\nu_1, \dots, \nu_{n-1}) = \int_0^\beta d^n \tau e^{i \sum_{i=1}^n \nu_i \tau_i} \mathcal{G}(\tau_1, \dots, \tau_n). \quad (7)$$

The Matsubara Green's function in Eq. (7) depends on $n - 1$ frequencies, since the time-translational invariance in imaginary-time equals a energy conservation in the Matsubara representation. Within this paper we label fermionic Matsubara frequencies with $\nu = \frac{\pi}{\beta}(2k + 1)$, respectively bosonic frequencies with $\omega = \frac{\pi}{\beta}2k$, where $k \in \mathbb{Z}$ and $\beta = 1/T$.

For a deeper discussion on the analytic properties of the multipoint correlators we refer to Ref. [35, 36].

A. Fermionic spectral function of the two-point correlation function

The spectral representation of the two-point Green's function is common textbook knowledge [1, 2]. Let us nonetheless recapitulated it here for comparison and better understanding of the more complicated spectral representation of the n -point correlator derived below. According to Eq. (2), the two-point fermionic correlator describes the following thermal averaged dynamical amplitude

$$G(\tau = \tau_1 - \tau_2) = -\langle T_\tau A(\tau) B(0) \rangle, \quad (8)$$

where we substituted $A_1 = A$ and $A_2 = B$ in Eq. (2). Following the former scheme and notation, the two-point correlator along the Matsubara frequency axis reads [2]

$$G(i\nu) = \int d\epsilon K_1(i\nu, \epsilon) \rho_1(\epsilon), \quad (9)$$

with the following kernel function and spectral density:

$$K_1(i\nu, \epsilon) = \int_0^\beta d\tau e^{i\nu\tau} K_1(\tau, \epsilon) = \frac{e^{-\beta\epsilon} + 1}{i\nu - \epsilon}, \quad (10)$$

$$\rho_1(\epsilon) = \int dt e^{i\epsilon t} \langle A(t) B(0) \rangle. \quad (11)$$

For $n = 2$, the imaginary part of the associated retarded correlation function yields the kernel spectral density:

$$\begin{aligned} \text{Im}[G(i\nu \rightarrow \nu + 0^+)] &= \text{Im}[G^R(\nu)] \\ &= -\pi [e^{-\beta\nu} + 1] \rho_1(\nu). \end{aligned} \quad (12)$$

which describes the linear response of a system to an external perturbation induced by operator B:

$$\begin{aligned} G^R(\nu) &= \int dt e^{i\nu t} G^R(t) \\ &= -i \int dt e^{i\nu t} \theta(t) \langle [A(t), B(0)]_+ \rangle. \end{aligned} \quad (13)$$

Eq. (9) shows that the imaginary- and real-time representation of the fermionic two-point correlator is connected by the bare fermionic Kernel $K^F(i\nu, \omega)$. This yields a Fredholm integral equation (9), which is rather difficult to solve and is a famous example for an inverse problem [37].

B. Spectral density representation of three-point correlator

In this section we investigate the spectral representation for the three-point Fermi-Bose vertex with two fermionic A, B and one bosonic C operator:

$$G(\tau_1, \tau_2) = \langle T_\tau A(\tau_1)B(\tau_2)C(0) \rangle. \quad (14)$$

This quantity forms the basis of several diagrammatic extensions of DMFT [22–25], and will be –besides the two-point correlator– at the focus of our NRG analysis below. There are two permutations, $\sigma_1 = (12)$ and $\sigma_2 = (21)$, for the time-ordering and thus according to the last section we can represent the imaginary-time Fermion-Boson vertex using two kernels and thermal spectral densities:

$$G(i\nu_1, i\nu_2) = \sum_{j=1}^2 \int d^2\epsilon K_j(i\nu_1, i\nu_2; \epsilon_1, \epsilon_2) \rho_j(\epsilon_1, \epsilon_2), \quad (15)$$

where the kernel functions are again the Matsubara Fourier transformed counterparts to the exponentially damped Heaviside step functions as in Eq. (5) for $n = 3$ which stem from the time-ordering and time-evolution. Performing the according integrals for the above kernel functions leads to

$$\begin{aligned} K_1(i\nu_1, i\nu_2; \epsilon_1, \epsilon_2) = & g^{sg}(\epsilon_1, \epsilon_2) \delta_{\nu_1+\nu_2,0} K^F(i\nu_1, \epsilon_1) \\ & + g_1^{FF}(\epsilon_1, \epsilon_2) K^F(i\nu_1, \epsilon_1) K^F(i\nu_2, \epsilon_2) \\ & + g_1^{FB}(\epsilon_1, \epsilon_2) K^B(i\nu_1 + i\nu_2, \epsilon_1 + \epsilon_2) \\ & \times [1 - \delta_{\nu_1+\nu_2,0}] K^F(i\nu_1, \epsilon_1) / (\epsilon_1 + \epsilon_2), \end{aligned} \quad (16)$$

and

$$\begin{aligned} K_2(i\nu_1, i\nu_2; \epsilon_1, \epsilon_2) = & g^{sg}(\epsilon_1, \epsilon_2) \delta_{\nu_1+\nu_2,0} K^F(i\nu_1, \epsilon_2) \\ & + g_2^{FF}(\epsilon_1, \epsilon_2) K^F(i\nu_1, \epsilon_1) K^F(i\nu_2, \epsilon_2) \\ & + g_2^{FB}(\epsilon_1, \epsilon_2) K^B(i\nu_1 + i\nu_2, \epsilon_1 + \epsilon_2) \\ & \times [1 - \delta_{\nu_1+\nu_2,0}] K^F(i\nu_2, \epsilon_1) / (\epsilon_1 + \epsilon_2), \end{aligned} \quad (17)$$

where

$$g^{sg}(\epsilon_1, \epsilon_2) = -\beta \delta_{\epsilon_1+\epsilon_2,0}, \quad (18)$$

$$g_1^{FF}(\epsilon_1, \epsilon_2) = e^{-\beta\epsilon_1} [1 + e^{-\beta\epsilon_2}], \quad (19)$$

$$g_2^{FF}(\epsilon_1, \epsilon_2) = -g_1^{FF}(\epsilon_2, \epsilon_1), \quad (20)$$

$$g_1^{FB}(\epsilon_1, \epsilon_2) = [1 - e^{-\beta(\epsilon_1+\epsilon_2)}] [1 - \delta_{\epsilon_1+\epsilon_2,0}], \quad (21)$$

$$g_2^{FB}(\epsilon_1, \epsilon_2) = -g_1^{FB}(\epsilon_1, \epsilon_2). \quad (22)$$

The kernel functions K_i can be represented as a linear combination of products of the bare fermionic [cf. Eq. (10)] and bosonic kernels labeled with F and B :

$$K^F(i\nu_n, \epsilon) = \frac{1}{i\nu_n - \epsilon}, \quad (23)$$

$$K^B(i\omega_n, \epsilon) = \frac{\epsilon}{i\omega_n - \epsilon}. \quad (24)$$

Each kernel function K_i is convolved with an associated spectral density

$$\rho_1(\epsilon_1, \epsilon_2) = \int d^2t e^{i\epsilon_1 t_1} e^{i\epsilon_2 t_2} \langle A(t_1)B(t_2)C(0) \rangle, \quad (25)$$

$$\rho_2(\epsilon_1, \epsilon_2) = \int d^2t e^{i\epsilon_1 t_1} e^{i\epsilon_2 t_2} \langle B(t_2)A(t_1)C(0) \rangle. \quad (26)$$

in order to yield the Green's function. Finally, we emphasize that the three-point Green's function separates into a singular (G_{sg}) and normal (G_{no}) part, where the former scales with the inverse temperature:

$$G(i\nu_1, i\nu_2) = \delta_{\nu_1+\nu_2,0} \beta G_{sg}(i\nu_1, i\nu_2) + G_{no}(i\nu_1, i\nu_2) \quad (27)$$

where

$$\begin{aligned} G_{sg}(i\nu_1, i\nu_2) = & - \int d^2\epsilon \delta_{\epsilon_1+\epsilon_2,0} K^F(i\nu_1, \epsilon_1) [\rho_1(\epsilon_1, \epsilon_2) + \rho_2(\epsilon_2, \epsilon_1)], \\ G_{no}(i\nu_1, i\nu_2) = & \int d^2\epsilon K^F(i\nu_1, \epsilon_1) K^F(i\nu_2, \epsilon_2) \sum_{i=1,2} g_j^{FF}(\epsilon_1, \epsilon_2) \rho_j(\epsilon_1, \epsilon_2) \\ & + \int d^2\epsilon [1 - \delta_{\nu_1+\nu_2,0}] K^B(i\nu_1 + i\nu_2, \epsilon_1 + \epsilon_2) \\ & \times [K^F(i\nu_1, \epsilon_1) g_1^{FB}(\epsilon_1, \epsilon_2) \rho_1(\epsilon_1, \epsilon_2) / (\epsilon_1 + \epsilon_2) \\ & + K^F(i\nu_2, \epsilon_1) g_2^{FB}(\epsilon_1, \epsilon_2) \rho_2(\epsilon_1, \epsilon_2) / (\epsilon_1 + \epsilon_2)]. \end{aligned}$$

Let us note that we could have also defined thermal densities following the lines of Ref. [31], given by $g^\alpha(\epsilon_1, \epsilon_2) \rho_i(\epsilon_1, \epsilon_2)$, where $\alpha \in \{sg, FF, FB\}$ and $i \in \{1, 2\}$. Within this notation the number of spectral densities increases as compared to Eq. (15), while they are convolved with the bare fermionic and bosonic kernel functions from Eq. (9).

III. MODEL AND METHOD

We compute the spectral densities for the single-orbital impurity Anderson model (SIAM)

$$\begin{aligned} H_{\text{SIAM}} = & \sum_{\sigma} \epsilon_d d_{\sigma}^{\dagger} d_{\sigma} + U d_{\uparrow}^{\dagger} d_{\uparrow} d_{\downarrow}^{\dagger} d_{\downarrow} \\ & + \sum_{k,\sigma} V_k [c_{k,\sigma}^{\dagger} d_{\sigma} + h.c.] + \sum_{k,\sigma} \epsilon_k c_{k,\sigma}^{\dagger} c_{k,\sigma}, \end{aligned} \quad (28)$$

where the localized impurity electrons are represented by the second quantization operators $\{d_{\sigma}, d_{\sigma}^{\dagger}\}$ with spin σ and interact with an effective Coulomb interaction U . The impurity electrons hybridize via V_k to bath degrees of freedom $\{c_{k,\sigma}, c_{k,\sigma}^{\dagger}\}$. The non-interacting bath has a dispersion ϵ_k such that the hybridization function is given by

$$\Delta(\omega) = \sum_k |V_k|^2 \delta(\omega - \epsilon_k). \quad (29)$$

We solve the impurity model with a NRG routine [38, 39]. Let us here only briefly summarize the procedure and refer for more details to [40, 41]. As a first step the conduction band is

divided up into logarithmic intervals $I_n^+ = [\varepsilon_{n+1}^+, \varepsilon_n^+]$ for $\omega > 0$, respectively $I_n^- = [\varepsilon_n^-, \varepsilon_{n+1}^-]$ for $\omega < 0$, using logarithmic discretization points $\varepsilon_n^\pm = \pm D \Lambda_{NRG}^{-n}$ with $n \in \mathbb{N}_0$ and $\Lambda_{NRG} > 1$ within the bandwidth D .

The conduction electron operators are then Fourier transformed within each logarithmic interval. It can be shown that thereby just the leading order term couples for a constant hybridization strength within each logarithmic interval to the impurity degrees of freedom. This approximation improves for decreasing Λ_{NRG} and recovers the continuum in the limit $\Lambda_{NRG} \rightarrow 1$. Thus, the discretized hybridization function is represented by weights such that the total norm is conserved. Next, the thus discretized Hamiltonian is mapped by a unitary transformation onto a semi-infinite chain:

$$H_{WC} = \sum_{\sigma} \epsilon_d d_{\sigma}^{\dagger} d_{\sigma} + U n_{\uparrow} n_{\downarrow} + V [f_{0,\sigma}^{\dagger} d_{\sigma} + h.c.] \quad (30)$$

$$+ \sum_{n=0,\sigma}^{\infty} t_n [f_{n+1,\sigma}^{\dagger} f_{\sigma} + h.c.] + \sum_{n=0,\sigma}^{\infty} g_n f_{n,\sigma}^{\dagger} f_{n,\sigma}.$$

This Hamiltonian describes fermions $\{f_{n,\sigma}, f_{n,\sigma}^{\dagger}\}$ that hop with amplitudes t_n along the semi-infinite Wilson chain with a site-index n and each with an onsite energy g_n , where the latter vanish for a symmetric hybridization function. The impurity just couples to the first site of the Wilson chain described by the following operator

$$f_{0,\sigma} = \frac{1}{V} \sum_k V_k c_{k,\sigma}. \quad (31)$$

For more details we refer to Ref. [41]. In case the hopping amplitudes decay exponentially along the Wilson chain, the eigenstate space can be iteratively truncated, keeping only the N_{keep} lowest eigenstates and adding one additional bath site at a time. This tridiagonalization procedure is in general not necessary, but saves computational cost [42].

The explicit computation of the spectral densities in Eq. (11) and (25)-(26) are performed along the full-density matrix (FDM) formalism introduced in Ref. [43]. The FDM formalism provides a self-contained representation of the spectral densities with a high accuracy regarding the conservation of the spectral norm. However, it neglects processes connecting different shells within the Wilson chain. Further details on the implementation are discussed in the subsequent sections.

IV. VALIDATION ON THE MATSUBARA AXIS

A. Atomic limit

In order to analyze the performance of our NRG implementation, we start with the Hubbard atom, which corresponds to an isolated s orbital with an effective Coulomb interaction U :

$$H_{ATOM} = \sum_{\sigma} \epsilon_d d_{\sigma}^{\dagger} d_{\sigma} + U d_{\uparrow}^{\dagger} d_{\uparrow} d_{\downarrow}^{\dagger} d_{\downarrow}. \quad (32)$$

The numerical calculations are performed for an interaction strength $U = 1.0$ and inverse temperature $\beta = 20$ with a local chemical potential $\epsilon_d = -U/2$ at half-filling.

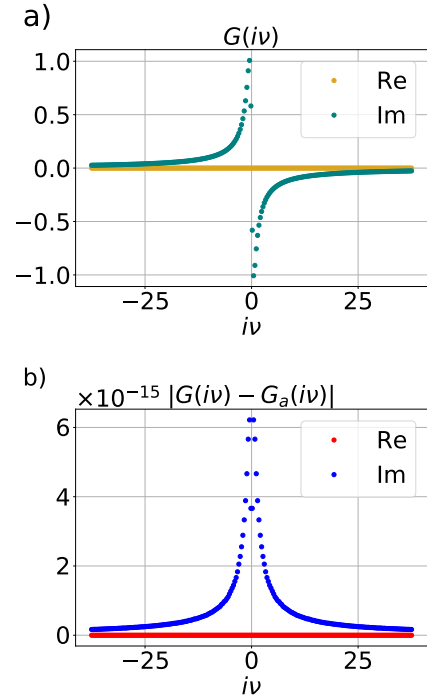


Figure 1. Two-point Green's function in the atomic limit at an inverse temperature $\beta = 20$, interaction strength $U = 1.0$, and half-filling. a) $G(iv)$ as calculated by NRG with $N_{keep} = 512$ and $\Lambda_{NRG} = 2.0$. b) Error vs. the exact $G_a(iv)$ [Eq. (35)].

1. Two-point spectral density

The imaginary-time spin-resolved Green's function reads

$$G_a(\tau) = -\langle T_{\tau} d_{\uparrow}(\tau) d_{\uparrow}^{\dagger}(0) \rangle. \quad (33)$$

In the atomic limit, the Anderson impurity can be solved analytically. Evaluating the spectral function yields

$$\rho_a(\omega) = \frac{1 + \exp[-\beta\epsilon_d]}{\mathcal{Z}} \delta(\omega - \epsilon_d) \quad (34)$$

$$+ \frac{\exp[-\beta\epsilon_d] + \exp[-\beta(2\epsilon_d + U)]}{\mathcal{Z}} \delta(\omega - \epsilon_d - U)$$

with the partition sum $\mathcal{Z} = \text{Tr}[e^{-\beta H}]$.

At half-filling and finite interaction strength the spectrum consists of two excitation peaks away from the Fermi level for the transitions from single to double and unoccupied impurity site, respectively. We convolve the kernels with the spectral functions to obtain the imaginary-time Green's function:

$$G_a(iv) = \int d\epsilon K^F(iv, \epsilon) \rho_a(\epsilon) \quad (35)$$

$$= \frac{1 + \exp[-\beta\epsilon_d]}{\mathcal{Z}} K^F(iv, \epsilon_d)$$

$$+ \frac{\exp[-\beta\epsilon_d] + \exp[-\beta(2\epsilon_d + U)]}{\mathcal{Z}} K^F(iv, \epsilon_d + U).$$

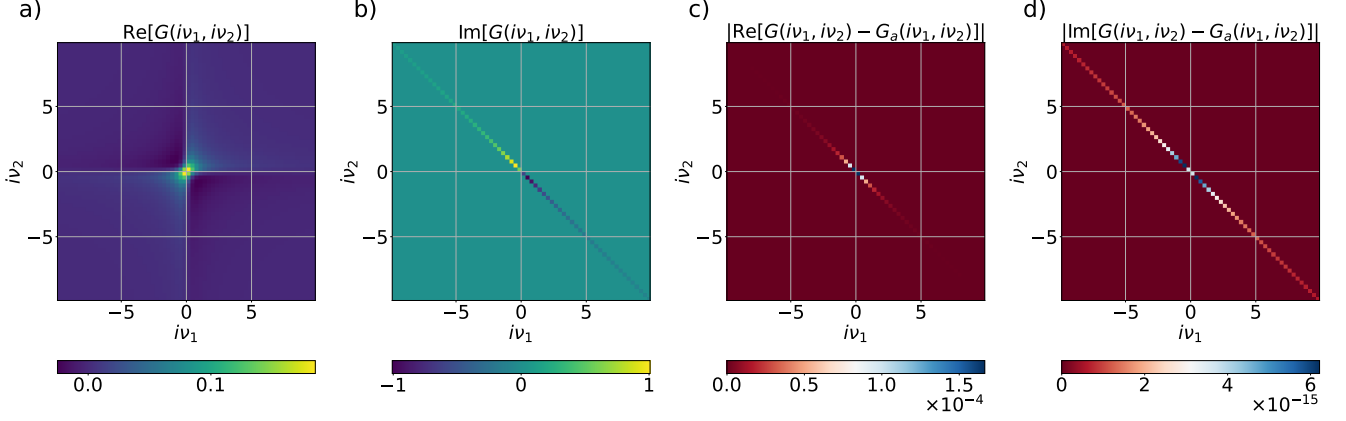


Figure 2. Three-point Green's function in the atomic limit for $\beta = 20$, $U = 1.0$, and half-filling: parts a) and b) show the real and imaginary part as calculated in NRG for $N_{keep} = 512$ and $\Lambda_{NRG} = 2.0$; parts c) and d) the difference to the exact result $G_a(i\nu_1, i\nu_2)$ [Eq. (36) ff.].

We plot in Fig. 1 a) the real and imaginary parts of the Green's function determined by NRG. Due to particle-hole symmetry the real part vanishes. As shown the imaginary part decreases for small Matsubara frequencies indicating that the original spectrum is insulating. In Fig. 1 b), we verify that analytic and numerical results are in excellent agreement.

2. Three-point spectral densities

Next we consider the local Fermi-Bose vertex

$$G_a(\tau_1, \tau_2) = \langle T_\tau d_\uparrow(\tau_1) d_\uparrow^\dagger(\tau_2) n(0) \rangle. \quad (36)$$

$$G_{a,no}(i\nu_1, i\nu_2) = -\frac{1}{\mathcal{Z}} \left[\left(1 + \exp[-\beta\epsilon_d] \right) \frac{1}{i\nu_1 - \epsilon_d} \frac{1}{i\nu_2 + \epsilon_d} + \left(\exp[-\beta(2\epsilon_d + U)] + \exp[-\beta\epsilon_d] \right) \frac{1}{i\nu_1 - \epsilon_d - U} \frac{1}{i\nu_2 + \epsilon_d + U} \right], \quad (39)$$

$$G_{a,sg}(i\nu_1, i\nu_2) = \frac{1}{\mathcal{Z}} \left[\exp[-\beta\epsilon_d] \frac{1}{i\nu_1 - \epsilon_d - U} + 2 \exp[-\beta(2\epsilon_d + U)] \frac{1}{i\nu_1 - \epsilon_d - U} + \exp[-\beta\epsilon_d] \frac{1}{i\nu_1 - \epsilon_d} \right]. \quad (40)$$

Part a) and b) in Fig. 2 show real and imaginary part of the three-point Green's function against the fermionic Matsubara frequencies. For $\beta = 20$ and $U = 1$, the real part is dominated by the normal Green's function, whereas the imaginary part mostly depends on the singular contribution to the Green's function. At half-filling normal and singular Green's function satisfy

$$G_{a,no}(i\nu_1, i\nu_2) = G_{a,no}(i\nu_2, i\nu_1), \quad (41)$$

$$G_{a,sg}(i\nu_1, i\nu_2) = -G_{a,sg}(i\nu_2, i\nu_1). \quad (42)$$

Comparison with the exact results, s. Fig. 2 c) and d), shows good agreement.

From Eq. (25) and (26) using a Lehmann representation we determine

$$\rho_{a,1}(\epsilon_1, \epsilon_2) = \frac{\exp[-\beta\epsilon_d]}{\mathcal{Z}} \delta(\epsilon_1 - \epsilon_d - U) \delta(\epsilon_2 + \epsilon_d + U), \quad (37)$$

$$\rho_{a,2}(\epsilon_1, \epsilon_2) = \frac{\exp[-\beta\epsilon_d]}{\mathcal{Z}} \delta(\epsilon_1 + \epsilon_d + U) \delta(\epsilon_2 - \epsilon_d - U) \quad (38)$$

$$+ \frac{\exp[-\beta(2\epsilon_d + U)]}{\mathcal{Z}} \delta(\epsilon_1 + \epsilon_d) \delta(\epsilon_2 - \epsilon_d).$$

Both spectral functions are centrosymmetric, i.e. $\rho_{a,i}(\epsilon_1, \epsilon_2) = \rho_{a,i}(-\epsilon_2, -\epsilon_1)$. As for the two-point correlator, we can separate the Fermi-Bose vertex into its normal and singular parts, i.e., $G_a = G_{a,no} + G_{a,sg}$ where

B. Comparison with Quantum-Monte Carlo

After comparing our method to an exact solution for a simple model, we now turn to the full SIAM as defined in Eq. (28). While no general analytic solution exists for the SIAM, quantum Monte Carlo (QMC) can, in principle, compute the result to arbitrary precision. In practice, however, the computational cost of the QMC algorithm scales unfavorably with decreasing temperature, which is not the case for the NRG procedure.

Here we benchmark our NRG result to QMC data as generated by the `w2dynamics` [44, 45] code, which uses continuous-time quantum Monte Carlo in the hybridization

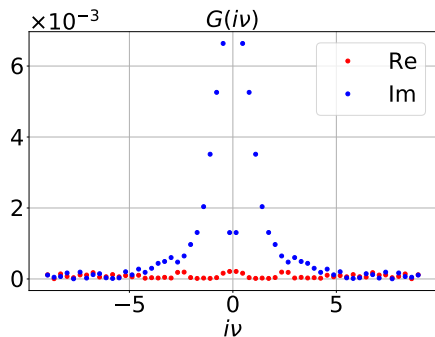


Figure 3. Absolute difference of the two-point correlator $G(iv)$ between the NRG (with $N_{keep} = 512$ and $\Lambda_{NRG} = 2.0$) and QMC solution for the SIAM at $U = 1.0$, $\beta = 20$, constant hybridization $\Delta = 0.1$ at half-filling. Real part (red) and imaginary part (blue). Statistical noise stems from QMC, while systematic deviations are from the NRG routine.

expansion [46] (CT-HYB). We measured all quantities using the worm-sampling method [47, 48] and used order 10^8 and 10^9 measurements for the two-point and three-point correlator, respectively.

For the AIM we choose a box shaped hybridization function [Eq. (29)] $\Delta(\omega) = \Delta\Theta(D - |\omega|)$, where the band-width $D = 1$ sets our unit of energy. We consider an interaction of $U = 1D$ and the half-filled case, which corresponds to $\epsilon_d = -U/2$. The two-point and three-point correlators, as defined in Eq. (9) and Eq. (15), are then measured at intermediate temperature $T = 1/20D$.

Fig. 3 and Fig. 4 display the absolute error between the QMC and NRG results for the two-point and three-point correlator, respectively. The background noise originates from the statistical error in the QMC data, while the structural deviation stems from NRG, which can mostly be observed in the low-frequency domain and along the anti-diagonal direction for the three-point function.

While QMC results can be improved by increasing the number of measurements, the NRG solution depends on the choice of N_{keep} and Λ_{NRG} . Table I displays the total absolute error between QMC and NRG as a function of N_{keep} , which confirms the expected improvement of the NRG approximation.

V. INTERMEDIATE REPRESENTATION

While it is difficult to find an effective discretization for the real frequency axis, due to the fact that the spectral function can be arbitrarily “peaky”, transitioning to the imaginary axis has a smoothing effect. This smoothing can be used to construct a rapidly converging representation.

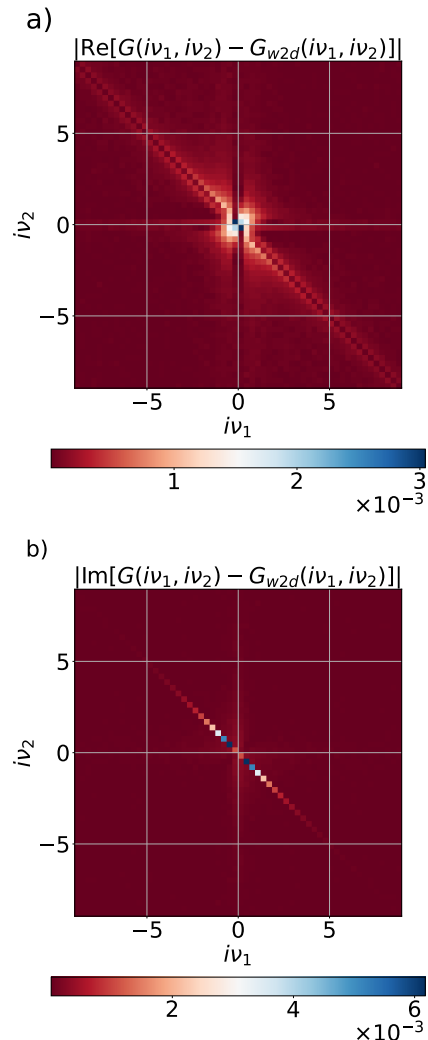


Figure 4. Absolute difference of the three-point correlator $G(iv_1, iv_2)$ between the NRG (with $N_{keep} = 512$ and $\Lambda_{NRG} = 2.0$) and QMC solution for the SIAM at $U = 1.0$, $\beta = 20$, constant hybridization $\Delta = 0.1$ at half-filling. a) Real part and b) imaginary part. Statistical noise stems from QMC, while systematic deviations are from the NRG routine.

We start by condensing Eqs. (8) and (13) to:

$$\begin{aligned} G(\tau) &= \frac{1}{\pi} \int d\epsilon \frac{e^{-\tau\epsilon}}{e^{-\beta\epsilon} \mp 1} \text{Im} G^R(\epsilon) \\ &= - \int d\epsilon \frac{e^{-\tau\epsilon}}{e^{-\beta\epsilon} \mp 1} \rho_1(\epsilon), \end{aligned} \quad (43)$$

where in the denominator we choose “-” for bosons and “+” for fermions. Frequently the kernel is represented by the dimensionless variables $x = \epsilon/\epsilon_{max} \in [-1, 1]$ and $y = \tau/\beta - \frac{1}{2} \in [-1, 1]$, with a characteristic parameter $\Lambda_{IR} = \beta\epsilon_{max}$. The integral kernel in Eq. (43) admits a singular value expansion [49]:

$$\frac{e^{-\tau\epsilon}}{e^{-\beta\epsilon} \mp 1} = \sum_{l=0}^{\infty} U_l^{\pm}(\tau) S_l^{\pm} V_l^{\pm}(\epsilon), \quad (44)$$

Table I. Total absolute error between the NRG and QMC result for the two-point (2pt) and three-point (3pt) correlator for the SIAM at $U = 1, \beta = 20$, half-filling, various N_{keep} of the NRG routine. For the error summation a box of ± 29 frequencies for each argument was chosen, which corresponds to the frequency-windows displayed in Fig. 3 and 4.

$\ \cdot\ _2$ [10^{-2}]		$\Lambda_{NRG} = 2.0$	
		2pt	3pt
N_{keep}	256	6.82	7.35
	512	3.01	3.20
	1024	1.38	1.61

where $\{S_l^\pm\}$ are the singular values in strictly decreasing order, $S_0 > S_1 > \dots > 0$, $\{U_l^\pm\}$ are the left singular functions, which form an orthonormal set on the imaginary-time axis; and $\{V_l^\pm\}$ are the right singular functions in Eq. (44), which form an orthonormal set on real frequencies. (For bosons, overlap on the real axis is understood with respect to the measure $d\mu = \epsilon d\epsilon$.)

The singular functions U_l^\pm and V_l^\pm in Eq. (44) are the so-called intermediate representation (IR) basis functions, which can be used as representation for the imaginary-time Green's function [30]:

$$G(\tau) = \sum_{l=0}^{L-1} U_l^\pm(\tau) G_l + E_L(\tau), \quad (45)$$

where $G_l = S_l \rho_l = S_l \int_\xi V_l(\epsilon) \rho(\epsilon)$ is a basis coefficient and E_L is an error term associated with truncating the series after L singular values. As shown in [50], S_l drops exponentially with l and grows only logarithmically with bandwidth in units of temperature [50]. One also observes that the right singular functions V_l are bounded, which implies the truncated representation (45) converges as $\log E_L^{-1} = \mathcal{O}(L/\log(\beta\epsilon_{max}))$ [50].

In order to efficiently extract the imaginary-frequency basis coefficients G_l from $G(\tau)$, we exploit the fact that the singular functions form a Chebyshev system [51], similar in structure to orthogonal polynomials. Hence, we choose a set of sampling points $\{\tau_1, \dots, \tau_L\}$ as the roots of the highest-order basis function $U_L(\tau)$ and turn Eq. (45) into an ordinary least squares fit [52]:

$$G_l = \arg \min_{G_l} \sum_{i=1}^L \left| G(\tau_i) - \sum_{l=0}^{L-1} U_l^\pm(\tau_i) G_l \right|^2. \quad (46)$$

One empirically observes that the design matrix in Eq. (46) is well-conditioned [52], implying that the fitting error is consistent with the overall truncation error E_L .

VI. REAL-AXIS IR REPRESENTATION OF SPECTRAL DENSITIES

A. Two-point correlator

As already mentioned, the IR basis is compact on the imaginary-time axis, since there the expansion coefficients G_l rigorously decay by virtue of the singular values S_l . Analytic expressions for the real axis are not known and the signal can be arbitrarily more complicated. The aim of this paper is to numerically analyze the prospects to use the IR coefficients also on the real axis. The expansion coefficients of the spectral function projected onto the real-frequency singular basis functions read

$$\rho_{j,l} = \int d\epsilon V_l(\epsilon) \rho_j(\epsilon), \quad (47)$$

with $l = 0, \dots, L-1$ in order to provide a compact basis on the real axis for a given precision target

$$\epsilon_{error} = S_L/S_0 \quad (48)$$

of the maximal (L 's) IR singular value (on the imaginary axis). Usually taking $L < L_{max}$ IR basis functions is sufficient thanks to their rapid decay on the imaginary axis. This means that real-frequency data which is directly available from the imaginary axis, such as the density or the spectral weight in an interval $\epsilon \in [-1/\beta, 1/\beta]$, is retained, whereas other spectral features are averaged over.

On the real axis, the truncation of ρ_l after L IR coefficients acts as a "smearing" filter when back-transformed to real frequencies:

$$\rho_{j,L}(\epsilon) := \int d\epsilon' \left[\sum_{l=0}^{L-1} V_l(\epsilon) V_l(\epsilon') \right] \rho_j(\epsilon'). \quad (49)$$

In order to get an intuition as to which features are smeared, we note that the right singular functions $\{V_l(\epsilon)\}$ also form a Chebyshev system [53]. Thus, there exists an associated Gauss quadrature rule on the real axis [54]. According to this, an integration over real frequency functions representable by a finite expansion in the basis set $\{V_l(\epsilon)\}$ equals a sum over the product of weights and the integrand evaluated at specific nodes. For ordinary polynomial basis functions, e.g. Legendre polynomials, the nodes are given by the roots of the highest polynomial needed to represent the function of interest and furthermore recursion relations for the weights exist. However, for a general Chebyshev system such as $\{V_l(\epsilon)\}$ the nodes and weights are a priori not known [54].

The density of the nodes of the highest computed IR basis function $V_{L_{max}}$ around some frequency ϵ is an indication of the resolution at that frequency. This means that smaller features in regions of more dense roots on the real axis have a more significant impact on the corresponding result on the imaginary axis. The zeros ϵ_i^* of V_L around $\epsilon = 0$ are approximately distributed as follows (cf. Fig. 5):

$$\epsilon_i^* = o(C \exp(-\alpha|i - L/2|)), \quad (50)$$

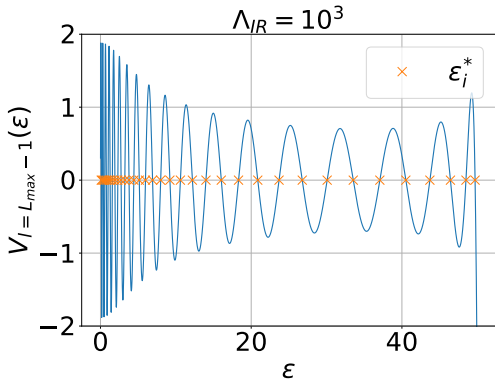


Figure 5. Highest IR basis function $V_{L_{max}}(\epsilon)$ for $\Lambda_{IR} = 10^3$. The density of its roots ϵ_i^* increases towards the Fermi energy. These roots are of special interest, since the IR basis function form a Chebyshev system (cf. main text).

where $\alpha \rightarrow 0.15(1)$ for $\Lambda_{IR} \rightarrow \infty$. The prefactor C actually scales approximately with $1/\Lambda_{IR}$ such that the density of roots close to the Fermi energy increase with smaller temperature and larger ϵ_{max} . In conclusion, a truncated expansion in $\rho_{j,l}$ is expected to preserve features close to the Fermi edge and smear out features far away from it, on par with observations in numerical analytical continuation [55].

The IR basis has already been shown to be extremely useful as compression tool on the imaginary axis [50]. In this paper we instead show how it can be applied to real-frequency objects. In the first step, we compute a discrete spectral function using our NRG routine. The peaky NRG spectrum is then broadened with a slightly modified version of the kernel proposed in Ref. [43]. The difference being an abrupt interpolation from Gaussian to log-Gaussian in our analysis:

$$\mathcal{K}_\alpha(\epsilon, \epsilon') = \begin{cases} K^G(\epsilon, \epsilon') & |\epsilon'| < \epsilon_0, \\ K_\alpha^{GL}(\epsilon, \epsilon') & |\epsilon'| \geq \epsilon_0, \end{cases} \quad (51)$$

with

$$\mathcal{K}^G(\epsilon, \epsilon') = \frac{1}{\sqrt{\pi\epsilon_0^2}} \exp(-(\epsilon - \epsilon')^2/\epsilon_0^2), \quad (52)$$

$$\mathcal{K}_\alpha^{GL}(\epsilon, \epsilon') = \frac{\theta(\epsilon\epsilon')}{|\epsilon| \sqrt{\pi\alpha^2}} \exp\left[-\left(\frac{1}{\alpha} \log\left|\frac{\epsilon}{\epsilon'}\right| - \frac{\alpha}{4}\right)^2\right]. \quad (53)$$

Here, the "smearing parameter" ϵ_0 depends on microscopic details of the NRG flow and, according to Ref. [43], is taken by a factor 2 smaller than the smallest energy scale in the system including also the Kondo temperature. The parameter α defines the broadening. Usually, in plain NRG calculations this parameter is set to $\alpha \sim 1/\sqrt{\Lambda_{NRG}}$, although it can be further reduced by using so-called z-shifts [42, 43]. In the following we analyze its impact on the compression. The broadened spectral function is then mapped onto the IR basis:

$$\rho_{j,l,\alpha} = \int d\epsilon \int d\omega \sum_{\omega_i} V_l(\epsilon) \mathcal{K}_\alpha(\epsilon, \omega_i) \rho_j(\omega), \quad (54)$$

where on the right hand side of this equation we consider the discrete spectral density $\rho_j(\omega)$ of (weighted) delta peaks at the excitation energies.

As shown Fig. 6 b), the real-frequency IR coefficients tend to decrease stronger for a greater broadening parameter α . To measure this on the frequency axis, we introduce the following norm and corresponding error:

$$\text{Err}_{rel}(L, \alpha)[\rho_j(\epsilon)] = \frac{\max_\epsilon |[\rho_{j,L,\alpha}(\epsilon) - \rho_{j,\alpha}(\epsilon)]|}{\max_\epsilon |\rho_{j,\alpha}(\epsilon)|}, \quad (55)$$

where $\rho_{j,L,\alpha}(\epsilon) = \sum_{l=0}^L L-1 \rho_{j,l,\alpha} V_l(\epsilon)$ is again the back-transform from the IR basis to real frequencies (for the two-point case $j = 1$). Later we also apply this measure to analyze the relative error of three-point functions. As expected the relative error shrinks with an increasing broadening parameter α , see Fig. 6 a). Furthermore, the two lower panels show how the reconstructed signal improves with an increasing number of real-frequency IR basis coefficients. Already with a rather small broadening $\alpha \approx 0.6$, a finite number of IR basis coefficients $L \approx 30$ suffice to store most of the information of the original signal (cf. Fig. 6). Below an upper boundary $\alpha < 0.7$, we empirically observe, using a least-square fit, that

$$\text{Err}_{rel}(L, \alpha)[\rho_1(\epsilon)] \sim c_1(\alpha) L^{c_2(\alpha)}, \quad (56)$$

where $c_1(\alpha)$ is approximately a quadratic and $c_2(\alpha)$ a linear functions of α . The fit has a root mean squared deviation of ≈ 0.14 and the maximum standard error on the fitting parameters is reasonable for the data set shown in Fig. 6.

For fitting the IR coefficients directly to real frequency data, as obtained e.g. from NRG, we rewrite the integral in Eq. (47) as a minimization problem, where we replace the integral by a sum over a finite number of frequency points ϵ_i :

$$\begin{aligned} \rho_{j,l,\alpha} &= \arg \min_{\rho_{j,\alpha}} \sum_{i=1}^{N_\epsilon} \left| \rho_{j,\alpha}(\epsilon_i) - \sum_{l=0}^{L-1} V_{il} \rho_{j,l,\alpha} \right|^2 \\ &= \sum_{i=1}^{N_\epsilon} V_{ii}^\oplus \rho_{j,\alpha}(\epsilon_i), \end{aligned} \quad (57)$$

where V^\oplus is the Moore–Penrose pseudoinverse of the matrix formed component-wise as $V_{il} = V_l(\epsilon_i)$ [56].

For computing the pseudoinverse, we analyze the condition number of the matrix V , which is minimized in case the set of frequencies ϵ_i includes a subset with roots of the highest singular value function $V_{L_{max}}(\epsilon)$. The number of roots ϵ_i^* is of the order of the highest polynomial L_{max} , and, for a fixed temperature and bandwidth, the highest polynomial in the IR basis that needs to be computed is given by $L_{max} \sim \log \Lambda_{IR} \log \epsilon_{error}^{-1}$ [57], where ϵ_{error} [Eq. (48)] describes the upper bound for the truncation error for the singular value decomposition. Thus, the spectral function can be reconstructed up to an error $\text{Err}_{rel}(L, \alpha)$ on a dense frequency grid starting from its values at the roots of the highest polynomial $V_L(\epsilon)$:

$$\rho_{j,\alpha}(\epsilon_i^*) = \int d\omega \mathcal{K}_\alpha(\epsilon_i^*, \omega) \rho_j(\omega) \quad (58)$$

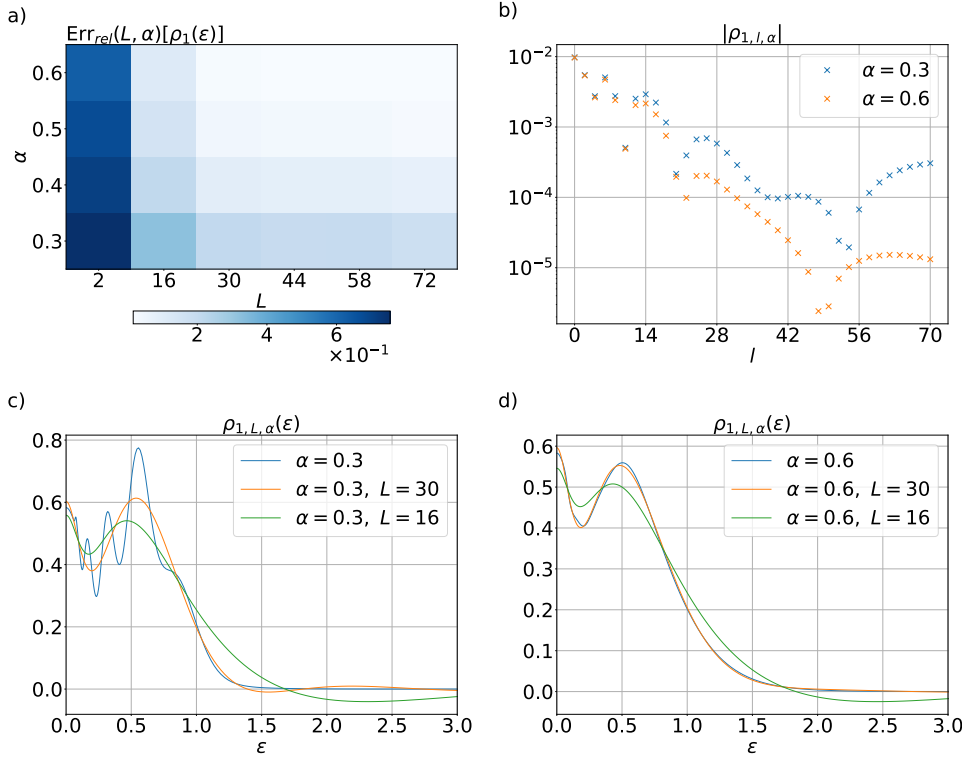


Figure 6. a) Relative error of the reconstructed two-point spectral density for the SIAM at $\beta = 20$, $U = 1.0$, constant hybridization $\Delta = 0.1$, $N_{keep} = 512$, $\Lambda_{NRG} = 2.0$ against the broadening parameter α and number of considered real-frequency IR basis coefficients L . With greater α and considering a larger IR basis space L , the error decreases. The further figures show additional information: b) Magnitude of expansion coefficient $\rho_{l,\alpha}$ over expansion coefficient l for two different broadenings α . The magnitude of the coefficients $\rho_{l,\alpha}$ shrinks with increasing broadening parameter α . c,d) We reconstruct the spectrum, keeping $L \in \{16, 30\}$ IR basis functions and compare it to the original broadened NRG spectrum with $\alpha \in \{0.3, 0.6\}$ (blue line).

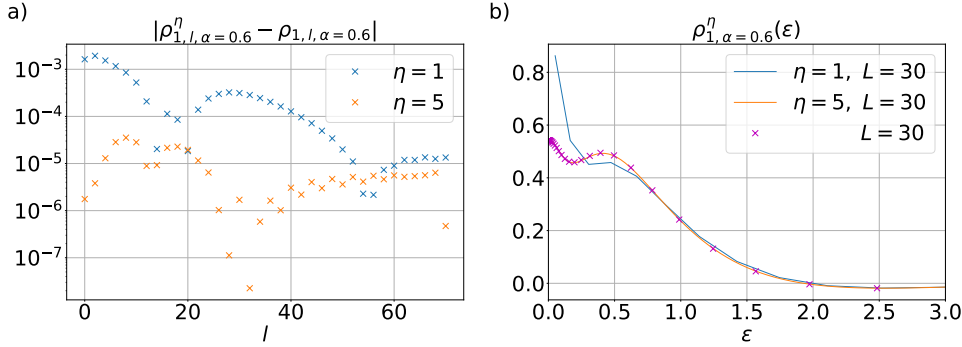


Figure 7. Thanks to the properties of the IR basis functions $V_l(\epsilon)$, only a small set of frequency points is needed to reproduce the original two-point function (same parameters as in Fig. 6). a) In order to verify this, we show that the real-frequency IR basis coefficients for a fixed broadening $\alpha = 0.6$ are well approximated for an oversampling factor $\eta = 5$. b) This figure verifies that already $\eta = 5$ is enough to yield the original signal along the real axis.

with the discrete NRG spectral density $\rho_j(\omega)$. The price for this reconstruction is a detour via the IR basis representation. We further consider an oversampling factor η according to which additional linearly separated points between each pair of adjacent roots, i.e. the total number of grid points used, yields approximately $N_\epsilon \approx L \eta$ frequencies. We mark this by adding a label to the broadened spectral density $\rho_\alpha^\eta(\epsilon)$, respectively the real-frequency IR basis coefficients $\rho_{l,\alpha}^\eta$. In case of $\eta = 1$, the set of frequency points equals the roots $V_{L,\alpha}(\epsilon_i^*) = 0$.

In Fig. 7 a), we compare the real-frequency IR basis coefficients thus computed from the solution of Eq. (57) for various oversampling factors to the integration of Eq. (54) on a very dense grid. It shows that with an increasing oversampling factor, the coefficients are closer to the result from the integral. On the real axis already $\eta = 5$ is sufficient to reproduce the

original signal (s. Fig. 7 b)).

Of course, this approach entails a trade-off. The more peaky the spectral function is, i.e. the lower a broadening parameter α is used, the harder it can be compressed and thus more IR basis coefficients are needed. Consequently the number of roots at which the spectral function in Eq. (58) needs to be known increases. Second, we mention that for $\alpha > 1.0$ (outside the range of Fig. 6) the results stagnate, i.e., the coefficients $\rho_{j,l,\alpha}$ are not further decreasing with increasing $\alpha > 0 \forall l$.

B. Three-point spectral function

We now turn to the three-point spectral function. As defined in Eq. (15), we restrict our analysis to the contribution that

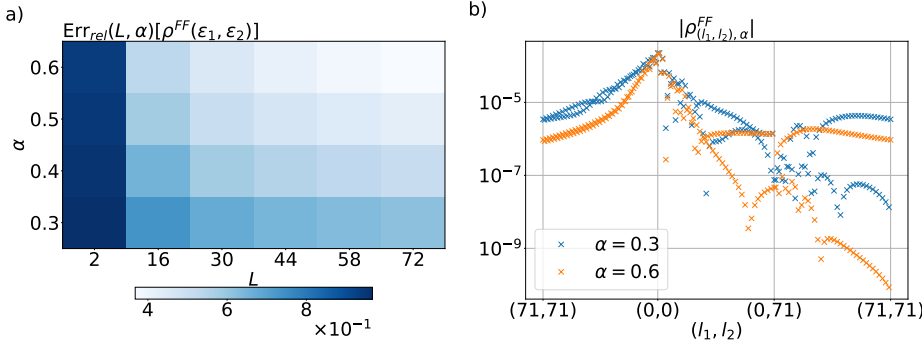


Figure 8. Relative error of the spectral density $\rho_{12}^{FF}(\epsilon_1, \epsilon_2)$ [cf. definition (59)] of the three-point spectral densities for the SIAM at $\beta = 20$, $U = 1.0$, $\Delta = 0.1$, half-filling, $N_{keep} = 512$ and $\Lambda_{NRG} = 2.0$. a) The discrete data is then broadened for a series of α and mapped onto the IR basis. The reconstructed signal, where we considered a finite number of IR basis coefficients L , is compared to the original spectral density by investigating the relative error. As discussed in the main text, the error reduces with greater broadening parameter α . b) Real-frequency coefficients, which have the tendency to be smaller for larger α .

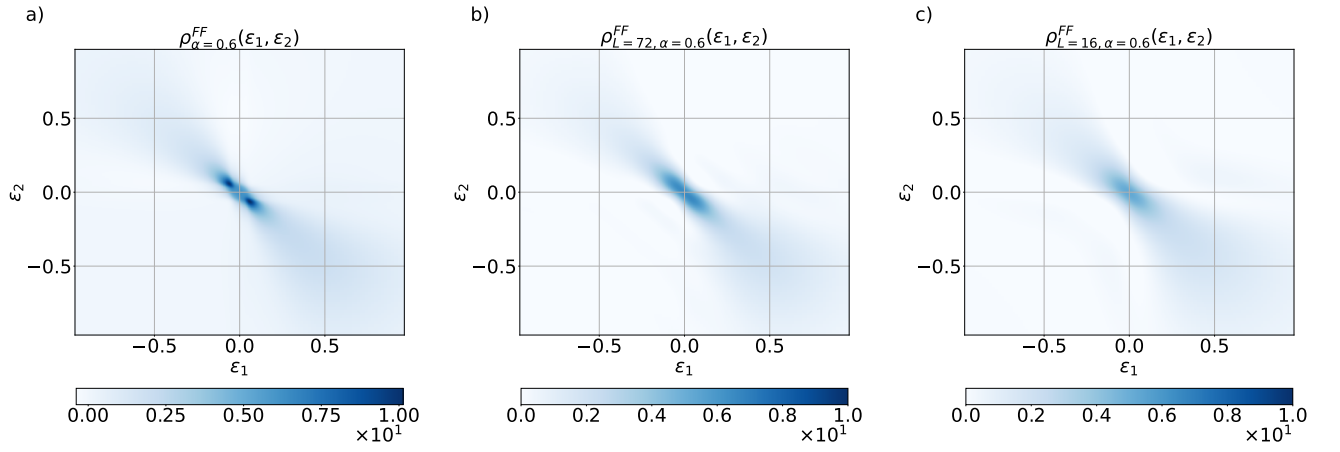


Figure 9. a) Original three-point spectrum ρ_{α}^{FF} after broadening the discrete NRG data with $\alpha = 0.6$ [cf. Eq. (60)]. b) and c) Reconstructed spectral density considering $L = 72$ and $L = 16$ IR basis coefficients, respectively, as given by Eq. (62). Close to the center $(\epsilon_1, \epsilon_2) = (0, 0)$ we observe a smearing of finer details in the IR reconstructed spectral function.

comes with two fermionic kernels:

$$\rho^{FF}(\epsilon_1, \epsilon_2) = \sum_{j \in \{1,2\}} g_j^{FF}(\epsilon_1, \epsilon_2) \rho_j(\epsilon_1, \epsilon_2). \quad (59)$$

Again we consider the broadened spectral density and investigate its compressibility in the IR basis against broadening:

$$\begin{aligned} \rho_{\alpha}^{FF}(\epsilon_1, \epsilon_2) \\ = \int d^2\omega \mathcal{K}_{\alpha}(\epsilon_1, \omega_1) \rho^{FF}(\omega_1, \omega_2) \mathcal{K}_{\alpha}(\omega_2, \epsilon_2) \end{aligned} \quad (60)$$

with the discrete spectrum $\rho^{FF}(\omega_1, \omega_2)$. We emphasize that this broadening kernel is not physically motivated, i.e. we did not investigate if such a kernel leads, among other things, to the correct asymptotics. This is left for future work. Here, we are interested instead in the connection between broadening and compression in the IR basis of such a three-point real-frequency correlator. Fig. 8 b) shows that the real-frequency

IR basis coefficients

$$\rho_{(l_1, l_2), \alpha}^{FF} = \int d^2\epsilon \rho_{\alpha}^{FF}(\epsilon_1, \epsilon_2) V_{l_1}(\epsilon_1) V_{l_2}(\epsilon_2) \quad (61)$$

have the tendency to be smaller for $\alpha = 0.6$ than for $\alpha = 0.3$. We further demonstrate in Fig. 8 that for $L = 72$, i.e.

$$\rho_{L=72, \alpha}^{FF}(\epsilon_1, \epsilon_2) = \sum_{l_1, l_2=0}^{71} \rho_{(l_1, l_2), \alpha}^{FF} V_{l_1}(\epsilon_1) V_{l_2}(\epsilon_2), \quad (62)$$

the relative error of the resulting signal compared to the original spectral density reduces to $\text{Err}_{rel}(L, \alpha) \approx 0.4$ for $\alpha = 0.6$.

In order to visualize the error in more detail and directly along the real frequency axis, we show in Fig. 9 the original data $\rho_{\alpha=0.6}^{FF}$ next to the reconstructed signal as e.g. given by Eq. (62). For $L = 72$ the form of the spectral density is roughly reproduced in panel b). However details of the original data shown in panel a) are smeared out, e.g. close to $(\epsilon_1, \epsilon_2) = (\pm 0.1, \mp 0.1)$. When reducing the number of considered IR basis coefficients to $L = 16$ as shown in part c),

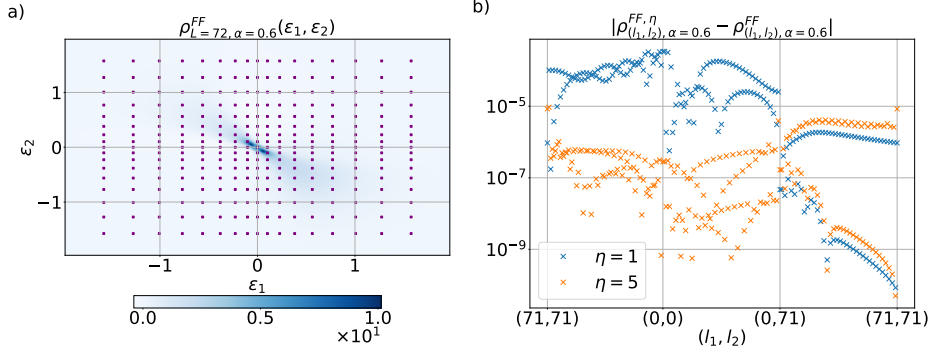


Figure 10. a) Spectral density ρ^{FF} defined in Eq. (59) (false color plot; same parameters as in Fig. 8) and roots of the highest polynomial $V_L(\epsilon_i^*) = 0$ (purple dots) at which the IR coefficients are computed. b) Comparison of the real-frequency coefficients of the original signal [shown in panel a)] to the spectral density evaluated obtained by minimizing Eq. (57) at $N_\epsilon = L\eta$ roots ϵ_i^* for oversampling parameter $\eta = 5$. The thus obtained IR coefficients for the three-point vertex deviate only slightly, maximally of the order of 10^{-5} .

this smearing becomes larger. According to this, the error between the original and reconstructed spectral densities reduces with increasing L . Altogether reproducing the three point vertex on the real axis with a reduced IR basis set appears to be more difficult than for the two-point function in Fig. 6. This might be because the three-point vertex is either in general more complex compared to the two-point case, or because its asymptotics or its steep drop off at small frequencies is more difficult to cover in the IR basis.

Following the approach for the two-point spectral function in Eq. (57), we evaluate the spectral density just on the roots of the highest IR basis polynomial and consider an additional oversampling factor η in order to add in-between additional frequency points.

That is, we minimize for the three-point correlator

$$\begin{aligned} & \rho_{j,(l_1,l_2),\alpha} & (63) \\ & = \arg \min_{\rho_{j,(l_1,l_2),\alpha}} \left| \rho_{j,\alpha}(\epsilon_{i_1}, \epsilon_{i_2}) - \sum_{l_1,l_2=0}^{L-1} V_{i_1,l_1} \rho_{j,(l_1,l_2),\alpha} V_{l_2,i_2}^\oplus \right|^2 \\ & = \sum_{i_1,i_2=1}^{N_\epsilon} V_{l_1,i_1}^\oplus \rho_{j,\alpha}(\epsilon_{i_1}, \epsilon_{i_2}) V_{l_2,i_2} \end{aligned}$$

using the definitions from Eq. (57). The results are presented in Fig. 10 a) shows the broadened spectral density, where we have marked the frequency points $(\epsilon_{i_1}^*, \epsilon_{i_2}^*)$ with $0 \leq i_1, i_2 \leq 71$ given by the roots of the highest order IR basis polynomial for $\Lambda_{IR} = 10^3$. In Fig. 10 b) we see that the absolute error of the real-frequency IR basis coefficients compared to the original value is reduced with η .

In summary, the IR basis on the real axis offers a possibility to compress the spectral density on the real axis. The rate of compression strongly depends on the smoothness of the data. For methods based on a diagonalization routine such as NRG, this is directly linked to the broadening kernel usually applied during the postprocessing routines. So far this is only an empirical observation, which needs to be further investigated.

VII. COMPACTIFICATION OF IMAGINARY-TIME CORRELATION FUNCTIONS

Finally, we analyze the two- and three-point imaginary-time correlation function using the IR basis representation. In the past the IR basis has been successfully used to compress data from diagrammatic or Monte Carlo approaches [58–70]. Compression of objects directly from the real-frequency axis has been unexplored previously in the literature. In this Section we cover how this compression reflects on the imaginary-time IR basis coefficients and the Matsubara-frequency two-point Green's function and three-point Fermion-Bose vertex.

A. Two-point correlator

The computation of the real-frequency IR basis coefficients on the real axis for various oversampling factors has already been discussed in the former sections and is shown in Fig. (7) for the two-point correlator.

We now multiply the coefficients $\rho_{l,\alpha=0.6}^\eta$ elementwise with the singular values S_l (cf. Eq. (45)) and display the result in Fig. 11 a) again in comparison with the result from Eq. (54). As expected the imaginary-frequency IR basis coefficients decay exponentially with increasing l in Fig. 11 a), and hardly deviate from their exact counterpart. Thus, the correlation function on the Matsubara axis is readily reconstructed by considering just a few imaginary-frequency IR basis coefficients. In Fig. 11 b) we show further that since the coefficients $G_{l,\alpha=0.6}^\eta$ for $\eta = 1$ compared to $\eta = 5$ differ on the order of 10^{-4} in Fig. 11 a), so do the two signals on the Matsubara frequency axis in Fig. 11 b).

B. Three-point correlator

Similarly, in Fig. 12 a) the imaginary-frequency coefficients of the three-point correlation function

$$G_{(l_1,l_2),\alpha=0.6}^{FF,\eta=10} = S_{l_1 l_2} \rho_{(l_1,l_2),\alpha=0.6}^{FF,\eta=10} \quad (64)$$

fall off very rapidly with their maximum at $l_1 = l_2 = 0$. Fig. 12 b) shows the comparison of the reconstructed signal, when

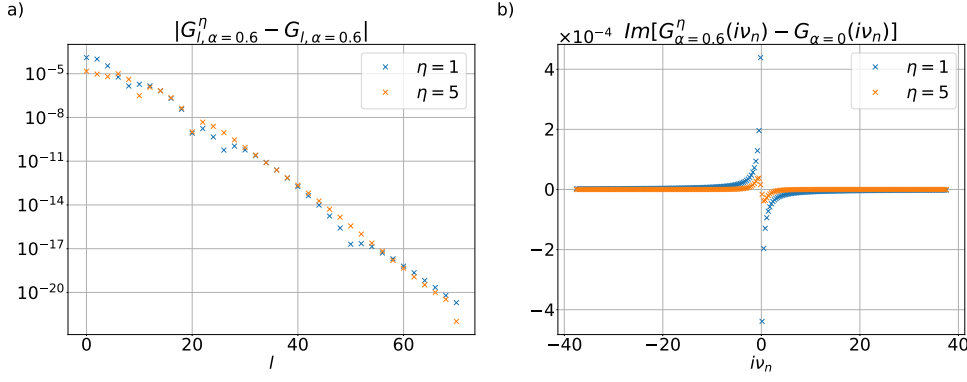


Figure 11. a) Error of the IR basis coefficients $G_{l,\alpha=0.6}^\eta$ compared to the exact solution for two oversampling factors $\eta \in \{1, 5\}$ in comparison to the result from Eq. (54) (parameters as in Fig. 7). The errors are rather similar. b) Absolute error of the two-point Matsubara frequency correlation function, which is of the order of 10^{-4} for $\eta = 1$ and 10^{-5} for $\eta = 5$.

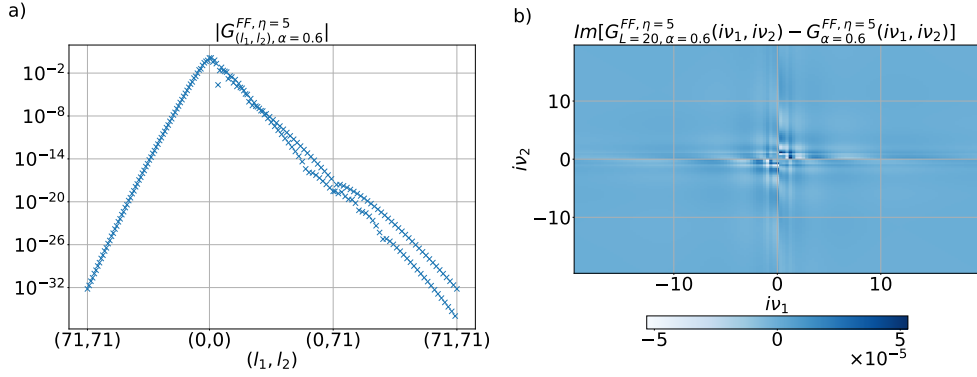


Figure 12. a) IR basis coefficients $G_{(l_1, l_2), \alpha=0.6}^{FF, \eta=5}$ (parameters as in Fig. 8). As expected from the exponential decrease of the singular values, the coefficients are largest close to $l_1 = l_2 = 0$. b) Additional error of the reconstructed three-point vertex if we restrict the IR basis subspace from $L = 72$ to $0 \leq l_1, l_2 \leq L = 20$. The absolute error is of the order of the corresponding IR coefficient $G_{(l_1=20, l_2=20), \alpha=0.6}^{FF, \eta=5}$ in panel a).

we consider just $L = 20$ coefficients for both l_1 and l_2 in comparison with the full correlation function. Specifically, we visualize the error $\text{Im}[E_L(i\nu_1, i\nu_2)]$ (equivalently defined as in Eq. (45), but for the three-point case and in Matsubara notation). The error is given by the magnitude of the coefficient $G_{(l_1=20, l_2=20), \alpha=0.6}^{FF, \eta=10}$, after which the IR basis is cut. Due to the structure of the correlation function, the error is largest for small Matsubara frequencies.

Figs. 11 and 12 empirically demonstrate that the concept of the IR basis is useful to systematically save storage space and computing time. Already the evaluation of the two-point real-frequency spectral function just on the roots of the largest real-frequency IR basis polynomial, i.e. for $\eta = 1$, is sufficient to represent the signal with high precision.

VIII. CONCLUSION

We have demonstrated the prospects of using the IR basis for real-frequency NRG data. On the imaginary axis, the singular-value decomposition of the imaginary-time kernel functions analytically guarantees an exponential convergence with the number of IR basis functions. For real times or frequencies such a rigorous theorem does not exist. We have,

however, demonstrated empirically that a compactification to L^2 data points with $L = 20 \dots 30$ IR basis functions is possible for the real-frequency two-point correlator. Requirement for a fast convergence is broadening the NRG delta-peaks. However only a broadening factor α commonly employed in NRG anyhow before z -shifts were introduced [42, 43] is needed.

In case of the three-point vertex it became obvious that the number of considered IR basis coefficients determines how well details of the spectral density are resolved. We have shown that for $L = 72$ the very peaky structure at small frequencies is smeared out. The form of the spectral density is still reproduced. Overall the tendency of the error reduction with increasing IR basis coefficients L holds.

Extrapolating the error, we expect to reconstruct the three-point vertex rather well for $L \approx 150$. The alternative is storing the n -point correlators directly at the iteratively calculated N NRG eigenfunctions [33], requiring N^{n-1} data. Usually in NRG, $N = 1000 \dots 10000$ is taken.[71] Using the IR basis results in a compactification by a factor of $(N/L)^{n-1}$, i.e., by the order of $10^{3(5)}$ for three(four)-point correlators.

ACKNOWLEDGMENTS

We thank Friedrich Krien, Fabian Kugler, Seung-Sup Lee, Jan von Delft, and Clemens Watzenböck for valuable discussions. This work has been supported by the FWF (Austrian Science Funds) through project P32044. Calculations have

been done in part on the Vienna Scientific Cluster (VSC).

Appendix A: Kernel spectral density representation

We start from the definition of the imaginary-time Green's function in Eq. (1) and here explicitly derive the kernel and spectral density representation of Eqs. (4)-(6):

$$\begin{aligned}
G(\tau_1, \dots, \tau_{n-1}) &= (-1)^{n+1} \langle T_\tau \left(\prod_{i=1}^{n-1} A_i(\tau_i) \right) A_n \rangle = \sum_{\sigma \in S_{n-1}} \text{sgn}(\sigma) (-1)^{n+1} \left(\prod_{i=1}^{n-2} \theta(\tau_{\sigma(i)} - \tau_{\sigma(i+1)}) \right) \left\langle \left(\prod_{i=1}^{n-1} A_{\sigma(i)}(\tau_{\sigma(i)}) \right) A_n \right\rangle \quad (\text{A1}) \\
&= \sum_{\sigma \in S_{n-1}} \text{sgn}(\sigma) (-1)^{n+1} \left(\prod_{i=1}^{n-2} \theta(\tau_{\sigma(i)} - \tau_{\sigma(i+1)}) \right) \left\langle \sum_{m_i} \frac{e^{-\beta E_{m_1}}}{\mathcal{Z}} \left(\prod_{i=1}^{n-1} \langle m_i | A_{\sigma(i)}(\tau_{\sigma(i)}) | m_{i+1} \rangle \right) \langle m_n | A_n | m_1 \rangle \right\rangle \\
&= \sum_{\sigma \in S_{n-1}} \text{sgn}(\sigma) (-1)^{n+1} \left(\prod_{i=1}^{n-2} \theta(\tau_{\sigma(i)} - \tau_{\sigma(i+1)}) \right) \left\langle \sum_{m_i} \frac{e^{-\beta E_{m_1}}}{\mathcal{Z}} \left(\prod_{i=1}^{n-1} \langle m_i | A_{\sigma(i)} e^{\tau_{\sigma(i)}(E_{m_i} - E_{m_{i+1}})} | m_{i+1} \rangle \right) \langle m_n | A_n | m_1 \rangle \right\rangle \\
&= \sum_{\sigma \in S_{n-1}} \text{sgn}(\sigma) (-1)^{n+1} \left(\prod_{i=1}^{n-2} \theta(\tau_{\sigma(i)} - \tau_{\sigma(i+1)}) \right) \left\langle \int_{\epsilon_i} \sum_{m_i} \frac{e^{-\beta E_{m_1}}}{\mathcal{Z}} \left(\prod_{i=1}^{n-1} \langle m_i | A_{\sigma(i)} e^{\tau_{\sigma(i)} \epsilon_i} | m_{i+1} \rangle \delta(\epsilon_i - (E_{m_i} - E_{m_{i+1}})) \right) \langle m_n | A_n | m_1 \rangle \right\rangle \\
&= \sum_{\sigma \in S_{n-1}} \text{sgn}(\sigma) (-1)^{n+1} \left(\prod_{i=1}^{n-2} \theta(\tau_{\sigma(i)} - \tau_{\sigma(i+1)}) \right) \int_{\epsilon_i} \left(\prod_{i=1}^{n-1} e^{\tau_{\sigma(i)} \epsilon_i} \right) \rho_\sigma(\epsilon_1, \dots, \epsilon_{n-1}) \\
&= \sum_{\sigma \in S_{n-1}} \text{sgn}(\sigma) \int_{\epsilon_i} K_\sigma(\tau_1, \dots, \tau_{n-1}; \epsilon_1, \dots, \epsilon_{n-1}) \rho_\sigma(\epsilon_1, \dots, \epsilon_{n-1}),
\end{aligned}$$

where $\{|m_i\rangle, E_{m_i}\}$ label eigenstates and corresponding eigenenergies of the Hamiltonian, which we introduced in the

second line of Eq. A1. We further introduced in the last two steps the generalized kernel and spectral density given by:

$$K_\sigma(\tau_1, \dots, \tau_{n-1}; \epsilon_1, \dots, \epsilon_{n-1}) = (-1)^{n+1} \left(\prod_{i=1}^{n-2} \theta(\tau_{\sigma(i)} - \tau_{\sigma(i+1)}) e^{-\epsilon_i \tau_{\sigma(i)}} \right) e^{-\epsilon_{n-1} \tau_{\sigma(n-1)}}, \quad (\text{A2})$$

$$\rho_\sigma(\epsilon_1, \dots, \epsilon_{n-1}) = \sum_{m_i} \frac{e^{-\beta E_{m_1}}}{\mathcal{Z}} \left(\prod_{i=1}^{n-1} \langle m_i | A_{\sigma(i)} | m_{i+1} \rangle \delta(\epsilon_i - (E_{m_i} - E_{m_{i+1}})) \right) \langle m_n | A_n | m_1 \rangle = \int_{t_i} \left\langle \left(\prod_{i=1}^{n-1} A_{\sigma(i)}(t_i) e^{i\epsilon_i t_i} \right) A_n \right\rangle. \quad (\text{A3})$$

- [1] A. Abrikosov, L. Gorkov, and I. Dzyaloshinskii, *Methods of Quantum Field Theory in Statistical Physics* (Dover, 1975).
- [2] G. Mahan, *Many-Particle Physics* (Kluwer Academic/Plenum Publishers, 2000).
- [3] F. Gebhard, *The Mott Metal-insulator transition* (Springer-Verlag (Berlin), 1997).
- [4] M. Imada, A. Fujimori, and Y. Tokura, Metal-insulator transitions, *Rev. Mod. Phys.* **70**, 1039 (1998).
- [5] P. Monthoux, A. V. Balatsky, and D. Pines, Toward a theory of high-temperature superconductivity in the antiferromag-

- netically correlated cuprate oxides, *Phys. Rev. Lett.* **67**, 3448 (1991).
- [6] A. Abanov, A. V. Chubukov, and J. Schmalian, Quantum-critical theory of the spin-fermion model and its application to cuprates: Normal state analysis, *Advances in Physics* **52**, 119 (2003), <https://doi.org/10.1080/0001873021000057123>.
- [7] Z. B. Huang, W. Hanke, E. Arrighoni, and A. V. Chubukov, Renormalization of the electron-spin-fluctuation interaction in the $t-t'-u$ hubbard model, *Phys. Rev. B* **74**, 184508 (2006).
- [8] F. Krien, P. Worm, P. Chalupa, A. Toschi, and K. Held, Spin

- scattering turns complex at strong coupling: the key to pseudogap and Fermi arcs in the Hubbard model, [arXiv:2107.06529 \(2021\)](#).
- [9] J. Frenkel, On the transformation of light into heat in solids. i, *Phys. Rev.* **37**, 17 (1931).
- [10] G. H. Wannier, The structure of electronic excitation levels in insulating crystals, *Phys. Rev.* **52**, 191 (1937).
- [11] B. L. Altshuler and A. G. Aronov, *Electron-Electron interaction in disordered conductors*, edited by A. I. Efros and M. Pollak (Elsevier Science Publisher, 1985).
- [12] A. Kauch, P. Pudleiner, K. Astleithner, P. Thunström, T. Ribic, and K. Held, Generic optical excitations of correlated systems: π -tons, *Phys. Rev. Lett.* **124**, 047401 (2020).
- [13] W. Metzner and D. Vollhardt, Correlated lattice fermions in $d = \infty$ dimensions, *Phys. Rev. Lett.* **62**, 324 (1989).
- [14] A. Georges and G. Kotliar, Hubbard model in infinite dimensions, *Phys. Rev. B* **45**, 6479 (1992).
- [15] A. Georges, G. Kotliar, W. Krauth, and M. J. Rozenberg, Dynamical mean-field theory of strongly correlated fermion systems and the limit of infinite dimensions, *Rev. Mod. Phys.* **68**, 13 (1996).
- [16] K. Held, O. Andersen, M. Feldbacher, A. Yamasaki, and Y. Yang, Bandstructure meets many-body theory: the lda+ dmft method, *Journal of Physics: Condensed Matter* **20**, 064202 (2008).
- [17] A. Toschi, A. A. Katanin, and K. Held, Dynamical vertex approximation; a step beyond dynamical mean-field theory, *Phys. Rev. B* **75**, 045118 (2007).
- [18] A. N. Rubtsov, M. I. Katsnelson, and A. I. Lichtenstein, Dual fermion approach to nonlocal correlations in the hubbard model, *Phys. Rev. B* **77**, 033101 (2008).
- [19] G. Rohringer, H. Hafermann, A. Toschi, A. A. Katanin, A. E. Antipov, M. I. Katsnelson, A. I. Lichtenstein, A. N. Rubtsov, and K. Held, Diagrammatic routes to nonlocal correlations beyond dynamical mean field theory, *Rev. Mod. Phys.* **90**, 025003 (2018).
- [20] A. A. Katanin, A. Toschi, and K. Held, Comparing pertinent effects of antiferromagnetic fluctuations in the two- and three-dimensional hubbard model, *Phys. Rev. B* **80**, 075104 (2009).
- [21] A. Galler, P. Thunström, J. Kaufmann, M. Pickem, J. M. Tomczak, and K. Held, The abinitiodga project v1.0: Non-local correlations beyond and susceptibilities within dynamical mean-field theory, *Comp. Phys. Comm.* **245**, 106847 (2019).
- [22] T. Ayrál and O. Parcollet, Mott physics and spin fluctuations: A functional viewpoint, *Phys. Rev. B* **93**, 235124 (2016).
- [23] E. A. Stepanov, Y. Nomura, A. I. Lichtenstein, and S. Biermann, Orbital isotropy of magnetic fluctuations in correlated electron materials induced by hund's exchange coupling, *Phys. Rev. Lett.* **127**, 207205 (2021).
- [24] F. Krien, A. Valli, P. Chalupa, M. Capone, A. I. Lichtenstein, and A. Toschi, Boson-exchange parquet solver for dual fermions, *Phys. Rev. B* **102**, 195131 (2020).
- [25] F. Krien, A. Kauch, and K. Held, Tiling with triangles: parquet and gw γ methods unified, *Phys. Rev. Research* **3**, 013149 (2021).
- [26] A. Valli, T. Schäfer, P. Thunström, G. Rohringer, S. Andergassen, G. Sangiovanni, K. Held, and A. Toschi, Dynamical vertex approximation in its parquet implementation: Application to hubbard nanorings, *Phys. Rev. B* **91**, 115115 (2015).
- [27] G. Li, A. Kauch, P. Pudleiner, and K. Held, The victory project v1.0: An efficient parquet equations solver, *Comp. Phys. Comm.* **241**, 146 (2019).
- [28] C. J. Eckhardt, G. A. H. Schober, J. Ehrlich, and C. Honerkamp, Truncated-unity parquet equations: Application to the repulsive hubbard model, *Phys. Rev. B* **98**, 075143 (2018).
- [29] N. Wentzell, G. Li, A. Tagliavini, C. Taranto, G. Rohringer, K. Held, A. Toschi, and S. Andergassen, High-frequency asymptotics of the vertex function: Diagrammatic parametrization and algorithmic implementation, *Phys. Rev. B* **102**, 085106 (2020).
- [30] H. Shinaoka, J. Otsuki, M. Ohzeki, and K. Yoshimi, Compressing Green's function using intermediate representation between imaginary-time and real-frequency domains, *Phys. Rev. B* **96**, 35147 (2017).
- [31] H. Shinaoka, J. Otsuki, K. Haule, M. Wallerberger, E. Gull, K. Yoshimi, and M. Ohzeki, Overcomplete compact representation of two-particle Green's functions, *Phys. Rev. B* **97**, 205111 (2018).
- [32] F. B. Kugler, S.-S. B. Lee, and J. von Delft, Multipoint correlation functions: Spectral representation and numerical evaluation, *Phys. Rev. X* **11**, 041006 (2021).
- [33] S.-S. B. Lee, F. B. Kugler, and J. von Delft, Computing local multipoint correlators using the numerical renormalization group, *Phys. Rev. X* **11**, 041007 (2021).
- [34] D. H. Kobe, Spectral representation of the many-time, causal Green's function in nonrelativistic many-body theory, *Ann. Phys.* **19**, 448 (1962).
- [35] A. Shvaika, On the spectral relations for multitime correlation functions, *Condens. Matter Phys.* **9**, 447 (2006).
- [36] A. Shvaika, Spectral properties of four-time fermionic Green's function, *Condens. Matter Phys.* **19**, 33004 (2016).
- [37] P. C. Hansen, *Discrete inverse problems: insight and algorithms* (SIAM, 2010).
- [38] K. G. Wilson, The renormalization group: Critical phenomena and the Kondo problem, *Rev. Mod. Phys.* **47**, 773 (1975).
- [39] H. Krishna-Murthy, J. Wilkins, and K. Wilson, Renormalization-group approach to the Anderson model of dilute magnetic alloys. i. Static properties for the symmetric case, *Phys. Rev. B* **21**, 1003 (1980).
- [40] A. Weichselbaum, Tensor networks and the numerical renormalization group, *Phys. Rev. B* **86**, 245124 (2012).
- [41] R. Bulla, T. A. Costi, and T. Pruschke, Numerical renormalization group method for quantum impurity systems, *Rev. Mod. Phys.* **80**, 395 (2008).
- [42] A systematic improvement of the energy resolution can be further achieved by introducing a z-shift parameter [72, 73]. Hereby, the discretization points are set to $\pm D\Lambda_{NRG}^{-(n+z)}$ with $z \in [0, 1]$ and we apply the above scheme for a fixed number N_z of z-shifts. Within this paper we do not consider z-shifts, although for future work it might be interesting to include this concept while optimizing the compression of data.
- [43] A. Weichselbaum and J. Von Delft, Sum-rule conserving spectral functions from the numerical renormalization group, *Phys. Rev. Lett.* **99**, 076402 (2007).
- [44] N. Parragh, A. Toschi, K. Held, and G. Sangiovanni, Conserved quantities of SU(2)-invariant interactions for correlated fermions and the advantages for quantum Monte Carlo simulations, *Phys. Rev. B* **86**, 155158 (2012).
- [45] M. Wallerberger, A. Hausoel, P. Gunacker, A. Kowalski, N. Parragh, F. Goth, K. Held, and G. Sangiovanni, w2dynamics: Local one- and two-particle quantities from dynamical mean field theory, *Computer Physics Communications* **235**, 388 (2019).
- [46] E. Gull, A. J. Millis, A. I. Lichtenstein, A. N. Rubtsov, M. Troyer, and P. Werner, Continuous-time Monte Carlo methods for quantum impurity models, *Rev. Mod. Phys.* **83**, 349 (2011).
- [47] P. Gunacker, M. Wallerberger, E. Gull, A. Hausoel, G. Sangiovanni, and K. Held, Continuous-time quantum Monte Carlo

- using worm sampling, *Phys. Rev. B* **92**, 155102 (2015).
- [48] P. Gunacker, M. Wallerberger, T. Ribic, A. Hausoel, G. Sangiovanni, and K. Held, Worm-improved estimators in continuous-time quantum Monte Carlo, *Phys. Rev. B* **94**, 125153 (2016).
- [49] P. C. Hansen, *Discrete Inverse Problems: Insights and Algorithms* (SIAM, 2010).
- [50] N. Chikano, J. Otsuki, and H. Shinaoka, Performance analysis of a physically constructed orthogonal representation of imaginary-time Green's function, *Phys. Rev. B* **98**, 035104 (2018).
- [51] M. Wallerberger, H. Shinaoka, and A. Kauch, Solving the Bethe–Salpeter equation with exponential convergence, *Phys. Rev. Research* **3**, 033168 (2021).
- [52] J. Li, M. Wallerberger, N. Chikano, C.-N. Yeh, E. Gull, and H. Shinaoka, Sparse sampling approach to efficient *ab initio* calculations at finite temperature, *Phys. Rev. B* **101**, 035144 (2020).
- [53] S. Karlin, *Total Positivity* (Stanford University Press, 1968).
- [54] V. Rokhlin and N. Yarvin, Generalized Gaussian quadratures and singular value decompositions of integral operators, *SIAM J. Sci. Comput.* **20**, 44 (1996).
- [55] R. K. Bryan, Maximum entropy analysis of oversampled data problems, *Eur. Biophys. J.* **18**, 165 (1990).
- [56] G. H. Golub and C. F. Van Loan, *Matrix Computations*, 3rd ed. (Johns Hopkins University Press, 1996).
- [57] N. Chikano, K. Yoshimi, J. Otsuki, and H. Shinaoka, *ir-basis*: Open-source database and software for intermediate-representation basis functions of imaginary-time Green's function, *Comput. Phys. Commun.* **240**, 181 (2019).
- [58] T. Nomoto, T. Koretsune, and R. Arita, Local force method for the *ab initio* tight-binding model: Effect of spin-dependent hopping on exchange interactions, *Phys. Rev. B* **102**, 014444 (2020).
- [59] T. Nomoto, T. Koretsune, and R. Arita, Formation mechanism of the Helical Q Structure in Gd-based Skyrmion Materials, *Phys. Rev. Lett.* **125**, 117204 (2020).
- [60] Y. Nomura, T. Nomoto, M. Hirayama, and R. Arita, Magnetic exchange coupling in cuprate-analog d^9 nickelates, *Phys. Rev. Research* **2**, 043144 (2020).
- [61] S. Isakov, C.-N. Yeh, E. Gull, and D. Zgid, *Ab initio* self-energy embedding for the photoemission spectra of NiO and MnO, *Phys. Rev. B* **102**, 085105 (2020).
- [62] N. Witt, E. G. C. P. van Loon, T. Nomoto, R. Arita, and T. O. Wehling, Efficient fluctuation-exchange approach to low-temperature spin fluctuations and superconductivity: From the Hubbard model to $\text{Na}_x\text{CoO}_2 \cdot y\text{H}_2\text{O}$, *Phys. Rev. B* **103**, 205148 (2021).
- [63] P. Pokhilko, S. Isakov, C.-N. Yeh, and D. Zgid, Evaluation of two-particle properties within finite-temperature self-consistent one-particle Green's function methods: Theory and application to GW and GF2, *J. Chem. Phys.* **155**, 024119 (2021).
- [64] C.-N. Yeh, S. Isakov, D. Zgid, and E. Gull, Electron correlations in the cubic paramagnetic perovskite $\text{Sr}(\text{V}, \text{Mn})\text{O}_3$: Results from fully self-consistent self-energy embedding calculations, *Physical Review B* **103**, 195149 (2021).
- [65] C.-N. Yeh, A. Shee, Q. Sun, E. Gull, and D. Zgid, Relativistic self-consistent GW: Exact Two-Component Formalism with One-Electron Approximation for Solids, [arXiv:2202.02252](https://arxiv.org/abs/2202.02252) (2022).
- [66] N. Witt, J. M. Pizarro, T. Nomoto, R. Arita, and T. O. Wehling, Doping fingerprints of spin and lattice fluctuations in moiré superlattice systems, [arXiv:2108.01121](https://arxiv.org/abs/2108.01121) (2021).
- [67] Y. Nagai and H. Shinaoka, Smooth Self-energy in the Exact-diagonalization-based Dynamical Mean-field Theory: Intermediate-representation Filtering Approach, *J. Phys. Soc. Jpn.* **88**, 064004 (2019).
- [68] Y. Nagai, Intrinsic vortex pinning in superconducting quasicrystals, [arXiv:2111.13288](https://arxiv.org/abs/2111.13288) (2021).
- [69] E. Itou and Y. Nagai, Qcd viscosity by combining the gradient flow and sparse modeling methods, [arXiv:2110.13417](https://arxiv.org/abs/2110.13417) (2021).
- [70] R. Sakurai, W. Mizukami, and H. Shinaoka, Hybrid quantum-classical algorithm for computing imaginary-time correlation functions, [arXiv:2112.02764](https://arxiv.org/abs/2112.02764) (2021).
- [71] For four-point correlators evaluated in [33] this albeit had to be somewhat reduced because of memory constraints.
- [72] V. L. Campo Jr and L. N. Oliveira, Alternative discretization in the numerical renormalization-group method, *Phys. Rev. B* **72**, 104432 (2005).
- [73] T. Pruschke *et al.*, Energy resolution and discretization artifacts in the numerical renormalization group, *Phys. Rev. B* **79**, 085106 (2009).